Ann. Geophys., 41, 327–337, 2023
https://doi.org/10.5194/angeo-41-327-2023

Annales Geophysicae Open Access EGU

Velocity of magnetic holes in the solar wind from Cluster multipoint measurements

Henriette Trollvik, Tomas Karlsson, and Savvas Raptis

School of Electrical Engineering and Computer Science, Division of Space and Plasma Physics, KTH Royal Institute of Technology, Stockholm, Sweden

Correspondence: Henriette Trollvik (trollvik@kth.se)

Received: 22 February 2023 – Discussion started: 24 February 2023
Revised: 22 May 2023 – Accepted: 28 May 2023 – Published: 21 August 2023

Abstract. We present the first statistical study on the velocity of magnetic holes (MHs) in the solar wind. Magnetic holes are localized depressions of the magnetic field, often divided into two classes: rotational and linear MHs. We have conducted a timing analysis of observations of MHs from the Cluster mission in the first quarter of 2005. In total, 69 events were used; out of these, there were 40 linear and 29 rotational MHs, where the limit of magnetic field rotation was set to 50°. The resulting median velocity was 7.4 ± 45 and $25 \pm 42\,\mathrm{km\,s^{-1}}$ for linear and rotational MHs, respectively. For both classes, around 70 % of the events had a velocity in the solar wind frame that was lower than the Alfvén velocity. Therefore, we conclude that within the observational uncertainties, both linear and rotational MHs are convected with the solar wind.

1 Introduction

Magnetic holes (MHs) were first reported by Turner et al. (1977) and were defined as localized depressions in the magnetic field magnitude. Turner et al. (1977) also divided MHs into two categories, based on the rotation of the magnetic field across the MH: the linear magnetic holes, which have little to no rotation, and the rotational magnetic holes, which have a significant rotation. This division is commonly used, although the angular limit of what is classified as linear versus rotational varies. Studies that only consider linear MHs use limits varying from 10 to 25° (Madanian et al., 2020; Sperveslage et al., 2000; Tsurutani et al., 2011; Briand et al., 2010; Volwerk et al., 2020; Winterhalter et al., 1994; Xiao et al., 2010; Zhang et al., 2008). Also, the temporal scales of MHs, regardless of their classification, have been reported to vary from a few seconds to several minutes (Karlsson et al., 2021; Madanian et al., 2020; Sperveslage et al., 2000; Turner et al., 1977; Volwerk et al., 2020; Winterhalter et al., 1994; Xiao et al., 2010; Zhang et al., 2008).

Suggested formation mechanisms of linear MHs range from being remnants of magnetic mirror-mode structures (Winterhalter et al., 1994) to non-linear Alfvén waves (Tsurutani et al., 2002). The latter mechanisms include right-handed polarized Alfvén waves (Buti et al., 2001) and phase-steepened Alfvén waves (Tsurutani et al., 2002). For the rotational MHs, the formation mechanism has been suggested to be related to slow magnetic reconnection (Turner et al., 1977) or remnants of solar coronal structures (Zurbuchen et al., 2001).

The mirror-mode instability results from a strong ion temperature anisotropy and results in the generation of quasi-periodic decreases or peaks in the magnetic field strength. These structures have no velocity in the plasma frame but are convected with the plasma velocity (Southwood and Kivelson, 1993; Horbury et al., 2004). If solar wind MHs are remnants of mirror-mode structures, they are therefore expected to be convected with the solar wind. Horbury et al. (2004) also point out that if linear magnetic holes are related to mirror-mode structures, we expect them to have a cylindrical structure.

If linear MHs originate from Alfvén waves, they should move with a velocity of the order of the Alfvén velocity in the solar wind frame. The velocity distribution should also exhibit a double hump, representing structures traveling at plus or minus the Alfvén velocity (Avinash and Zank, 2007).

Rotational MHs have been less investigated over the years. Turner et al. (1977) connect the observations of rotational MHs with directional discontinuities (D sheets) associated with a magnetic field decrease (Gosling, 2012), first observed by Burlaga (1968). The D sheet is suggested to be the result of reconnection triggered by the large magnetic shear associated with the current sheath (Gosling, 2012). For larger rotational MHs (not kinetic scale), Zurbuchen et al. (2001) suggest that they are created from a magnetic flux tube in the corona reconnecting with an open magnetic field line. In both cases, the theory involves current sheet-like discontinuities.

An important open question regarding magnetic holes is determination of their velocities in the solar wind frame. This is important for two reasons:

1. Knowing the velocity, we can calculate the spatial scales of the MHs; furthermore, any uncertainty in the velocity determination will directly translate into spatial-scale uncertainties.

2. As described above, some theories predict a non-zero velocity with respect to the solar wind. Determining the propagation velocities will be a test of these and other non-mirror-mode theories.

Here we present the first statistical study investigating the velocity of solar wind MHs. This is done by applying multi-spacecraft timing techniques to Cluster data (Harvey, 1998). A similar method was used by Horbury et al. (2004) to investigate the propagation velocity of the magnetic mirror-mode structures in the magnetosheath. Below we will describe the methodology for such a velocity determination, show its results, and relate the derived velocities to the local Alfvén velocity and the magnetic field rotation of the magnetic holes.

2 Method

The Cluster mission consists of four spacecraft (S/C): C1, C2, C3, and C4. We have used observations from the first quarter of 2005. In this period, the S/C separations were between 562 and 2552 km, and most of the MHs passed all four S/C with a large enough time difference that the timing method can be used. In this period, the S/C also had orbits with apogee in the solar wind, spending about 30 % of the orbital time there. We use data from the following instruments. Firstly, a fluxgate magnetometer (FGM) (Balogh et al., 1997) for the magnetic field was used to identify the MH and the time difference between S/C. The full resolution of the magnetic field is 0.04 s. For ion velocity, we used the cluster ion spectrometer (CIS) (Rème et al., 2001) with a resolution of 4 s, primarily the hot ion analyzer (HIA), but in the absence of HIA data, we used the composition and distribution function analyzer (CODIF). To calculate the Alfvén velocity, we obtained the electron density from the waves of high frequency and sounder for probing of electron density

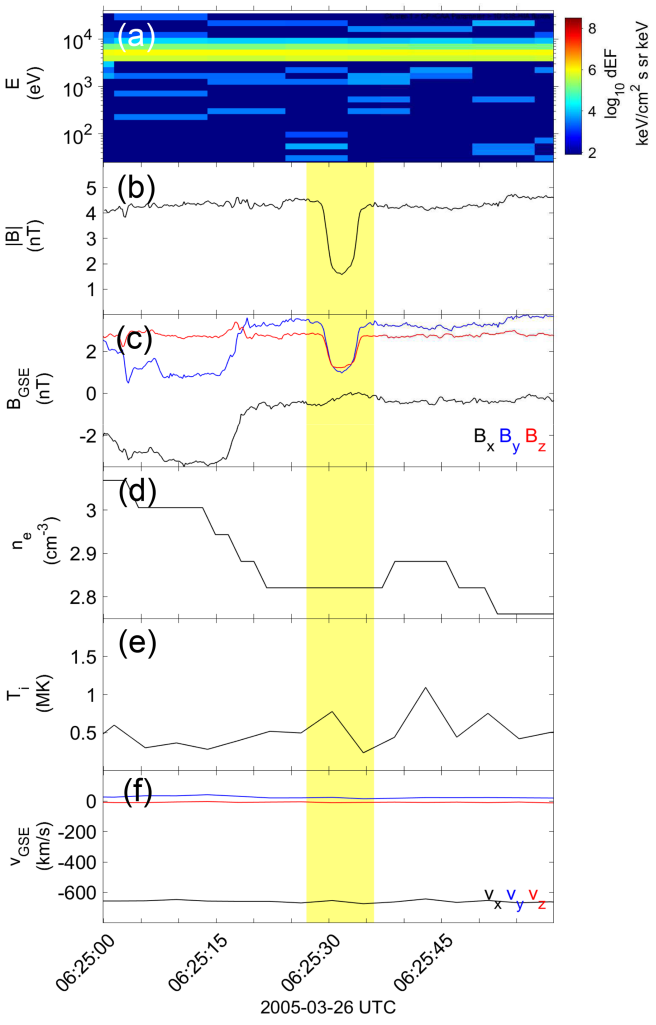

Figure 1. General parameters of a linear MH observed by C1. **(a)** Ion energy spectrum (HIA), **(b)** magnetic field magnitude (FGM), **(c)** C1 magnetic field components (FGM), **(d)** electron (WHISPER) and ion density (HIA), **(e)** ion temperature (HIA), and **(f)** velocity (HIA). The position of the S/C was [8.18, 0.05, 6.09] R_E. Velocity and magnetic field are in geocentric solar ecliptic (GSE) coordinates. The yellow shaded area indicates the MH region.

by relaxation (WHISPER) experiment (Décréau et al., 1997) with a resolution of 2.2 s.

2.1 Event identification

In this study, we are only interested in MHs located in the pristine solar wind. The solar wind regions were identified by first searching for regions where the cone angle ($\arctan(|\sqrt{v_y^2+v_z^2}/v_x|)$) of the velocity is smaller than 20°. To remove more turbulent regions, such as foreshock regions, we only consider MHs in regions where the normalized standard deviation of the magnetic field 30 s before and after the MH is less than 0.15. We define the normalized standard de-

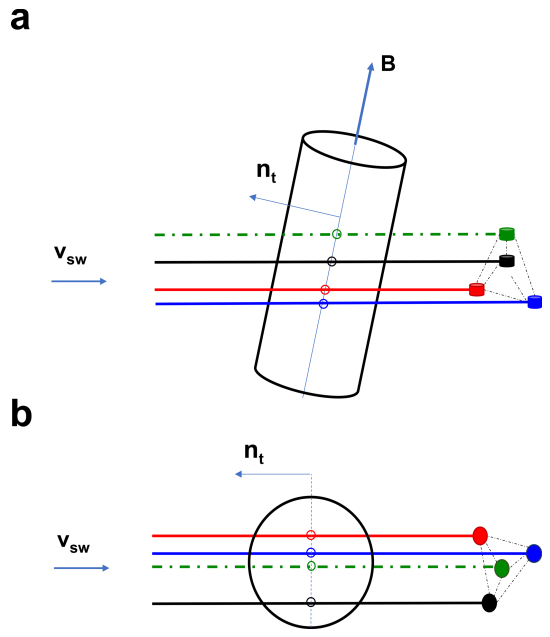

Figure 2. Panel **(a)** gives a 3D illustration of the configuration between MH and S/C. Panel **(b)** shows the 2D view from the top. The colors refer to typical Cluster S/C colors of black, red, green, and blue for C1, C2, C3, and C4. The figure is adapted from Horbury et al. (2004).

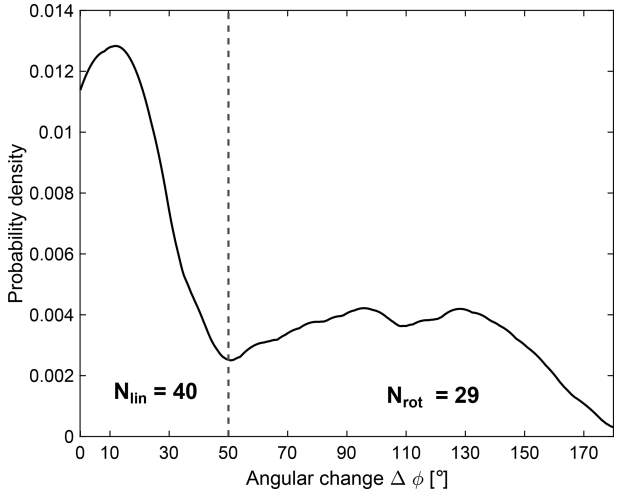

Figure 3. Probability density distribution of the change of the magnetic field across the MH. The vertical line indicates the limit for rotational and linear MHs.

viation as B_{SD}/B_0, where B_{SD} is the moving standard deviation, calculated with a 300 s window, and B_0 is defined below. Since MHs will cause an increase in the normalized standard deviation, the threshold is set high enough to filter out most of the turbulent regions but low enough for MHs to pass. As a result, some turbulent/foreshock regions are not excluded automatically. Such regions are often associated with high-energy ion populations. By visually inspecting the energy spectrogram, we removed these foreshock events. This visual inspection also ensures that we have correctly excluded magnetosheath intervals and only consider isolated MHs and not wave trains, like mirror modes.

In this paper, we have defined MHs as a structure fulfilling Eq. (1), i.e., having at least a 50 % reduction in magnetic field strength. This is similar to many other studies (e.g., Karlsson et al., 2021; Volwerk et al., 2020). The background field B_0 is obtained using a 5 min sliding window. The relative change in $\boldsymbol{B}$ is smoothed using a 1 s long sliding window to remove high-frequency waves and noise.

$$B_{\mathrm{rel}} = \frac{\Delta B}{B_0} = \left\langle \frac{|\boldsymbol{B}| - B_0}{B_0} \right\rangle_{1\,\mathrm{s}} < -0.5 \quad (1)$$

$$B_0 = \langle |\boldsymbol{B}| \rangle_{300\,\mathrm{s}} \quad (2)$$

We perform this process for all S/C. The last condition we impose is that the MH should be observed by all four S/C, which is determined by a visual inspection of the events.

Figure 1 shows an MH centered in a 1 min window from 26 March 2005 observed by C1. Figure 1a shows the ion energy flux from the CIS-HIA instrument plotted on a logarithmic scale. Here we see the narrow distribution, typical for the solar wind. Figure 1b and c show the magnetic field magnitude and its components in GSE coordinates. The magnetic field decreases from ∼4 to ∼2 nT, during a short interval, otherwise staying relatively constant. The Y and Z components decrease from the background magnitude and return to a similar level after passing the MH, while the X component remains unchanged. This example is a typical observation of a linear MH in the solar wind. In Fig. 1d, the electron density is shown. Figure 1e shows the ion temperature. The density and temperature increase inside the MH, suggesting total pressure balance, as has been reported before (e.g., Volwerk et al., 2020). Figure 1f shows the ion velocity in GSE.

2.2 Timing analysis

We can determine the velocity of the MHs when localized events are found. We have applied the method described in Harvey (1998) and used for Cluster observations of mirror modes by Horbury et al. (2004). Sundberg et al. (2015) also applied a similar technique for subproton-scale MHs in the terrestrial plasma sheet.

As mentioned in Sect. 1, it is believed that rotational MHs are sheet-like discontinuities, while linear MHs are solenoid-like structures. The method we will use is typically used for a planar discontinuity. Suppose, however, that magnetic holes have a cylindrical shape. The timing method will then produce a normal in the plane containing the solar wind flow direction and the magnetic field direction, as described by Horbury et al. (2004). Figure 2 shows an illustration of the geometry of the S/C in relation to a linear MH. The plane perpendicular to the flow velocity is defined by the magnetic field minimum. This illustrates that events where the S/C ob-

serve different levels of magnetic field strengths are applicable to the timing method. The same methodology was used by Horbury et al. (2004) on mirror-mode structures.

Knowing the times t_i and positions r_i for the MH minimum for spacecraft i, we get a system of equations for the timing normal vector $\hat{\boldsymbol{n}}_\mathrm{t}$ (Eq. 3), which is solved by introducing the "slowness" vector $\boldsymbol{m}$ (Eq. 4), resulting in Eq. (5).

$$v_t(t_j - t_i) = (r_j - r_i) \cdot \hat{\boldsymbol{n}}_\mathrm{t} \tag{3}$$

$$\boldsymbol{m} = \frac{\hat{\boldsymbol{n}}_\mathrm{t}}{v_t} \tag{4}$$

$$(t_j - t_i) = (r_j - r_i) \cdot \boldsymbol{m} \tag{5}$$

In principle, Eq. (5) can be easily solved by picking one of the spacecraft as the reference spacecraft. A more symmetric treatment, however, is to consider Eq. (5) as an overdetermined system of equations and determine the structure velocity by minimizing a quadratic error expressed in Eq. (6). Here N is the total number of S/C, and $\mathbf{R}$ is the volumetric tensor, defined in Eq. (7). $t_{\alpha\beta} = t_\alpha - t_\beta$ is the time difference between S/C, determined by cross correlation, and $k, l = x, y, z$ summation over repeated indices is assumed. The cross correlation was always very high, due to the MHs being isolated. A detailed description of this method can be found in Harvey (1998). This method is not valid when the S/C configuration is coplanar.

$$m_l = \frac{1}{2N^2}\left[\sum_{\alpha=1}^{N}\sum_{\beta=1}^{N} t_{\alpha\beta}(r_{\alpha k} - r_{\beta k})\right] R_{kl}^{-1} \tag{6}$$

$$R_{jk} = \frac{1}{N}\sum_{\alpha=1}^{N} r_{\alpha j} r_{\alpha k} \tag{7}$$

To determine the structure velocity in the plasma frame, we apply Eq. (8). Here $\boldsymbol{v}_\mathrm{sw}$ is the solar wind velocity, determined from HIA. From the timing method, we only obtain the velocity along the timing normal; thus, to find the velocity in the plasma frame, we take the projection of the solar wind velocity along the timing normal.

$$v_\mathrm{pf} = v_t - \boldsymbol{v}_\mathrm{sw} \cdot \hat{\boldsymbol{n}}_\mathrm{t} \tag{8}$$

As addressed in many previous papers investigating the velocities of structures, there can be large uncertainties. We have applied a similar technique as Horbury et al. (2004) and Wang et al. (2020) to estimate the error. The two main sources of error are the determination of the time difference and the solar wind velocity measurement (Knetter, 2005). For the time difference, we have taken the uncertainty to be two data points (~ 0.09 s). There are six unique combinations of S/C with corresponding time differences. For each of these, we add two data points before and after, resulting in an array of five points for each S/C. This results in a total of 15 625 unique combinations of S/C and time steps. We then find v_t by taking the mean of all results, and the error is determined by the standard deviation. The velocity error in the solar wind frame is obtained by applying the error propagation formula. We have assumed that the error in the Y and Z components of the solar wind is negligibly small and that the error of the X component is 10 %, similar to what was used by Wang et al. (2020).

In this study we will investigate linear and rotational holes separately. Figure 3 shows the probability density function of the change of the magnetic field over the MH, $\Delta\phi$, for the events used in this study. The rotation is determined from the angle between the mean magnetic field 10 s before and 10 s after the MHs. The probability density is estimated using the kernel density estimation (KDE), a non-parametric way to derive the probability density of a univariate distribution (Rosenblatt, 1956). The distribution shows a clear peak at 13°, with a tail extending to angles approaching 180°. The vertical line at 50° indicates the boundary set for linear and rotational MHs, resulting in 40 linear and 29 rotational MHs. The boundary was set based on the distribution and by visually inspecting the MH with $25 \leq \theta \leq 60$. This angular distribution is similar to what has been shown in previous studies (e.g., Karlsson et al., 2021). The mean temporal-scale size, determined by the full width at half minimum, of the 69 events was 5.9 s, with 5.4 s for linear and 6.8 s for rotational MHs.

3 Results

Using the method described in Sect. 2.1, we identified 72 MH events suitable for this study. However, only 69 will be used, as 3 were excluded due to the S/C configuration being close to coplanar, and the timing method is not applicable. In Appendix A, a table of all the events (including the three excluded ones) can be found, accompanied by the derived velocities and general parameters. Figure 4a–e show an example event of a linear MH from 31 March 2005, with a magnetic field rotation of 5°. Figure 4a shows the magnetic field magnitude in all four S/C, in Cluster colors (black, red, green, and blue for C1, C2, C3, and C4, respectively). We see that the MH is first seen by C4, followed by C3, C1, and C2. Figure 4b shows the same as Fig. 4a but shifted in time (cross correlated) so that the magnetic minima are aligned. Figure 4c shows the magnetic field components in GSE for S/C 4. Both the Y and Z components show a strong decrease, while the X component is more or less constant. Figure 4d and e show the S/C positions in X–Y and X–Z projections, respectively, in units of R_E (6371 km). For this event, there was a minimum and maximum S/C separation of 919 and 1333 km, respectively. In addition, the background magnetic field direction is indicated by the black arrow and the timing normal by the red one. The solar wind velocity measured by HIA for this event was $\boldsymbol{v}_\mathrm{sw} = [-465 \pm 47, 20, 9.8]\,\mathrm{km\,s^{-1}}$. The calculation of the timing normal using the method described above resulted in $\hat{\boldsymbol{n}}_\mathrm{t} = [-0.93 \pm 0.007, -0.28 \pm 0.018, 0.24 \pm 0.016]$. The angle between the normal

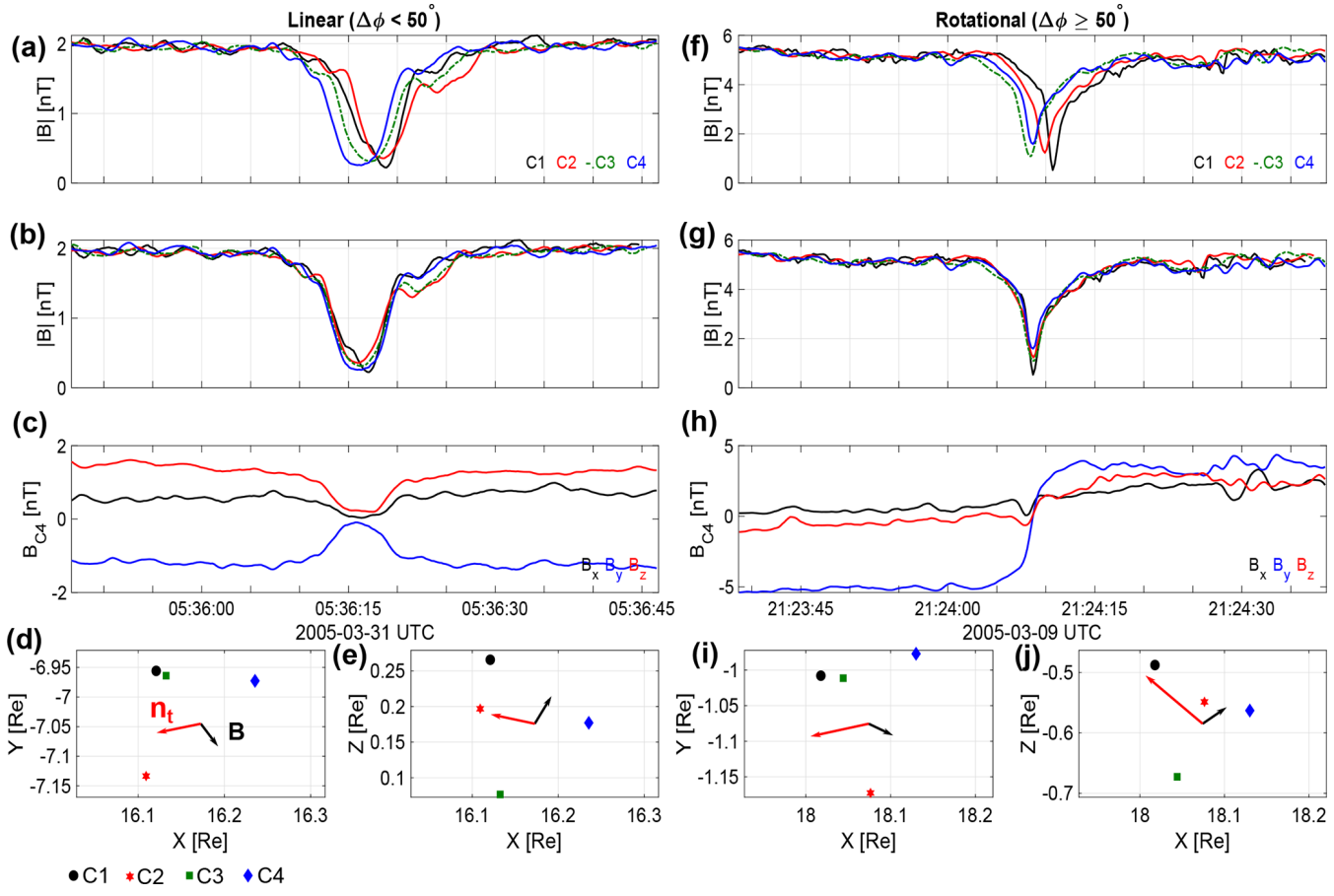

Figure 4. Example event of a linear **(a)**–**(e)** and a rotational **(f)**–**(j)** MH. Panel **(a)** shows the magnetic field magnitude observed in all S/C. Panel **(b)** shows the same as **(a)** but with the S/C time shifted according to C4. Panel **(c)** shows the magnetic field observed by C4. S/C position in the X–Y plane is given in panel **(d)**, while **(e)** shows the position in X–Z, both in the GSE coordinate system. Both the last panels have the magnetic field and timing normal plotted in black and red, respectively. Panels **(f)**–**(j)** have the same format as **(a)**–**(e)**.

vector and the solar wind velocity was $22.7 \pm 0.4°$, and the velocity in the normal direction $v_t = 432 \pm 8.76\,\mathrm{km\,s^{-1}}$. Using Eq. (8) we find the velocity in the solar wind frame to be $V_{pf} = 3.5 \pm 44\,\mathrm{km\,s^{-1}}$. The errors are estimated as described in Sect. 2.2, and we can see that the error increases significantly for the velocity in the plasma frame. This is due to the assumed high error of the solar wind velocity. For this event, the Alfvén velocity was $12.3\,\mathrm{km\,s^{-1}}$.

We also show an example of a rotational MH from 9 March 2005 in Fig. 4f–j, with the same format as Fig. 4a–e. Here we can see a clear rotation of 137° of the magnetic field vector over the MH. For this event, there was a minimum and maximum S/C separation of 899 and 1076 km, respectively. The normal vector was found to be $\hat{\boldsymbol{n}}_t = [-0.64 \pm 0.017, -0.17 \pm 0.014, 0.75 \pm 0.015]$. This is equivalent to an angle of $49 \pm 1.6°$ with the solar wind velocity, $\boldsymbol{v}_{sw} = [-680 \pm 68, 46, 24]\,\mathrm{km\,s^{-1}}$. The velocity in the normal direction was $422 \pm 7.9\,\mathrm{km\,s^{-1}}$, and using Eq. (8), we determine the velocity in the plasma frame to be $v_{pf} = -12 \pm 43\,\mathrm{km\,s^{-1}}$. For this event, the Alfvén velocity was $60.1\,\mathrm{km\,s^{-1}}$.

The results of the timing analysis applied to the whole dataset of MHs are shown in Fig. 5. Figure 5a and b show the results for the linear and Fig. 5c and d for the rotational MHs. The top panels show the MH velocities in the solar wind frame in the form of KDEs, and the bottom panel shows the MH velocity in the solar wind frame normalized with the Alfvén velocity. Considering the top panels first, we can see that the distributions for linear and rotational MHs are both centered close to zero. The median MH velocity in the solar wind frame is 7.4 ± 45 and $25 \pm 42\,\mathrm{km\,s^{-1}}$ for linear and rotational MH, respectively, while the mean is 19 and $27\,\mathrm{km\,s^{-1}}$. In Fig. 5, the median and the mean Alfvén velocity are indicated with vertical lines, and the horizontal bar shows the error. For comparison, we obtain the mean velocity in the timing frame v_t to be $436 \pm 10\,\mathrm{km\,s^{-1}}$.

To better see the relation between the MH velocity and the Alfvén velocity, the bottom panels show the MH velocity in the solar wind frame, normalized to the Alfvén velocity. The blue lines show $V_{pf}/V_A = \pm 1$, and the median and error are shown in red. The majority of the distribution lies within the

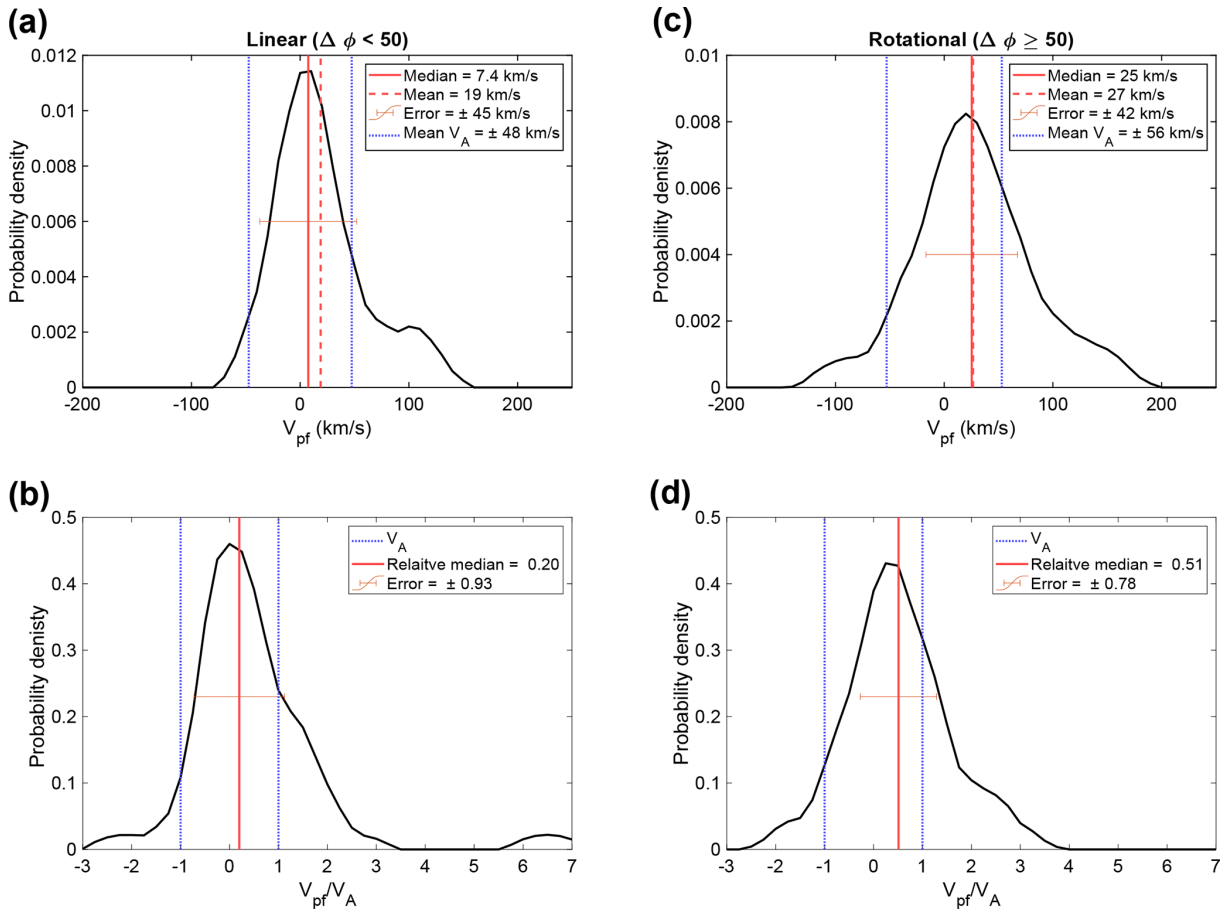

Figure 5. Probability density of the results, for **(a)**–**(b)** linear MHs and for **(c)**–**(d)** the rotational MHs. Panels **(a)** and **(c)** show the results as a function of the MH velocity in the plasma frame. Panels **(b)** and **(d)** show the results for the MH velocity relative to the mean Alfvén velocity.

Alfvén boundaries, with $\sim 78\,\%$ and $\sim 67\,\%$ for linear and rotational MHs, respectively.

4 Discussion and conclusions

The level of uncertainty in this study is mainly determined by the uncertainties of the solar wind velocity. We have used an error of 10 %, the same as in Wang et al. (2020), in the x direction and neglected the error in the other two components. As a result, the error will be larger for the events with higher solar wind velocity.

For the determination of the time shift, we choose a cross-correlation method. Another way would be to identify the minimum for all four S/C and directly take the difference. The linear MH shown in Fig. 3 is a good example of why this method would not be a good fit for some events. In C4 one sees that it does not have the exact same shape as the other three S/C. The minimum is a bit displaced, which would result in the wrong time shift, an error which would propagate to the velocity and normal determination. This could also affect the determination from the cross correlation, but we account for this in our error estimate.

Comparing the velocity to the local Alfvén velocity, we can see that the majority of the MHs, $\sim 70\,\%$ for both rotational and linear MHs, have velocities below the Alfvén velocity. We also see no sign of a double peak distribution, which we would expect if MHs move with the Alfvén velocity. The double peak distribution arises from structures moving with positive (towards Earth) or the negative (away from Earth) Alfvén velocity.

Our results are consistent with both rotational and magnetic holes convecting with the solar wind plasma. This is consistent with linear MH originating from mirror-mode instabilities. Our results are comparable to what was found by Horbury et al. (2004) for mirror-mode structures in the magnetosheath, where they also concluded that these structures are convected with the plasma. Wang et al. (2020) studied foreshock structures with a technique similar to the one we used here. They found a clear peak centered around $100\,\mathrm{km\,s^{-1}}$, indicating that the method used here can detect

structures not convecting with the solar wind plasma. This supports our conclusion that MHs move with the solar wind.

For rotational MHs, theories suggest that they are the result of magnetic reconnection events and are similar to D sheets, which should propagate with the solar wind. The rotational MHs have a median velocity of a factor of 3 larger than the linear ones but still small enough to be consistent with convection with the solar wind.

Concluding that MHs are convected with the plasma, the next step will be to derive scale sizes, since we can now confidently convert temporal-scale sizes to spatial ones. In addition, the results presented here provide an estimate of the errors of the spatial scales as well. With the Cluster mission, we have identified several observations of MHs where the S/C passes different parts of the structure, which can be used to derive the limits of these scales. In the future, we plan to investigate the morphology of the MHs, starting with the linear MHs, by combining observations with different models, such as the one used by Goodrich et al. (2021). As a follow-up study, the velocity of isolated MHs in the magnetosheath should be measured and compared with this study and the results of Horbury et al. (2004).

Appendix A

Table A1. List of all MHs used in this study with results, including identified outliers.

yyyy	mm	dd	hh	mm	ss	V_t	$V_{t,err}$	V_{sw}	V_{pf}	$V_{pf,err}$	$\Delta\varphi$	θ	QG	QR
2005	1	12	13	27	3.0	691.1	21.4	654.5	93.1	66.3	18.2	23.8	2.59	0.78
2005	1	15	1	45	30.7	439.3	9.2	606.8	−39.5	52.0	40.1	37.8	2.13	0.53
2005	1	15	2	14	56.6	504.3	18.1	649.1	68.0	58.5	77.1	47.6	2.06	0.48
2005	1	15	2	21	36.6	301.8	4.2	628.0	−73.9	48.1	148.2	53.2	2.04	0.47
2005	1	17	9	28	29.1	450.7	16.9	630.7	−43.9	50.3	5.8	38.3	2.33	0.65
2005	1	28	21	7	9.3	398.4	6.8	387.2	25.4	35.8	8.1	15.5	2.98	0.99
2005	1	29	9	54	55.9	383.6	5.9	425.9	−0.5	42.5	37.3	25.2	1.86	0.32
2005	1	30	14	30	53.9	431.3	8.3	580.3	13.5	45.9	14.4	43.9	2.93	0.97
2005	1	5	8	43	43.0	761.8	34.0	674.1	118.1	73.0	127.8	17.0	2.76	0.87
2005	2	10	0	10	22.7	400.9	6.2	682.1	13.5	44.1	5.6	55.4	2.79	0.89
2005	2	10	1	27	28.0	393.8	6.8	695.2	141.6	34.5	134.1	68.7	2.66	0.82
2005	2	10	3	28	18.3	605.8	24.9	698.0	52.3	53.8	9.6	37.4	2.40	0.69
2005	2	11	13	20	20.6	488.9	8.7	617.7	−3.6	46.2	53.3	37.1	2.89	0.95
2005	2	14	13	30	21.1	286.9	3.6	389.8	63.3	24.4	118.2	54.9	2.99	0.99
2005	2	14	9	32	29.6	233.1	3.0	350.4	−12.7	27.1	93.0	45.4	2.91	0.95
2005	2	17	3	41	9.0	393.4	4.9	384.8	36.3	37.5	1.5	21.8	2.75	0.87
2005	2	19	19	49	49.6	251.6	9.6	498.5	39.4	31.1	151.0	64.7	1.80	0.27
2005	2	19	19	57	41.2	458.1	21.2	509.1	0.1	45.5	3.0	25.3	1.78	0.25
2005	2	21	20	13	35.4	170.1	1.4	380.4	−27.3	17.7	5.8	58.7	2.88	0.93
2005	2	21	21	10	35.6	370.2	4.5	375.9	5.0	37.4	0.7	13.6	2.81	0.90
2005	2	25	16	12	43.3	355.7	4.7	548.0	3.9	39.2	146.7	50.0	2.99	0.99
2005	2	25	18	31	59.9	135.1	0.6	523.0	36.1	8.9	52.9	79.1	2.93	0.97
2005	2	26	9	26	13.5	247.7	2.8	535.2	−4.1	21.1	21.5	61.9	2.97	0.99
2005	2	28	21	56	55.4	633.7	15.6	614.9	56.6	60.5	78.3	19.8	2.95	0.97
2005	2	28	5	37	18.2	570.4	15.2	598.8	24.2	55.3	167.2	23.8	2.87	0.94
2005	2	2	18	40	17.4	354.3	4.8	501.4	−8.0	39.9	58.7	43.6	2.94	0.97
2005	2	2	18	50	9.1	605.1	16.3	518.9	124.7	47.8	6.2	22.1	2.93	0.96
2005	2	2	19	37	26.9	515.2	10.6	519.1	3.6	52.0	37.5	9.5	2.89	0.94
2005	2	4	16	11	21.4	169.1	1.4	441.3	25.3	14.7	121.8	71.0	2.81	0.92
2005	2	7	18	59	30.4	530.3	9.4	670.7	−6.0	60.7	4.8	36.8	2.33	0.64
2005	2	7	6	26	32.5	313.6	4.7	413.9	27.3	30.5	2.4	46.2	2.91	0.96
2005	2	9	18	24	58.0	648.6	18.9	685.3	28.0	63.8	0.8	25.0	2.98	0.99
2005	2	9	21	5	43.8	491.0	9.8	688.8	22.5	52.0	78.8	47.1	2.97	0.98
2005	2	9	23	46	44.2	667.6	18.1	729.5	5.9	66.9	103.1	24.7	2.82	0.90
2005	2	9	23	48	16.0	390.8	6.3	729.5	29.0	43.5	103.1	60.3	2.82	0.90
2005	2	9	2	38	57.9	521.7	10.7	725.6	35.3	51.2	117.8	47.9	2.94	0.97
2005	3	10	6	20	1.6	631.3	21.1	664.5	110.9	55.2	5.3	38.4	2.96	0.98
2005	3	10	6	56	41.5	337.8	5.2	670.4	44.8	29.7	109.7	64.1	2.97	0.99
2005	3	10	7	6	31.3	382.2	6.3	636.2	81.2	25.0	2.1	61.8	2.97	0.99
2005	3	12	1	19	27.4	244.7	2.2	435.3	0.7	22.5	24.8	55.9	2.92	0.96
2005	3	1	5	57	58.2	631.1	15.0	620.8	30.8	60.4	4.3	14.0	2.10	0.50
2005	3	23	19	31	11.2	335.0	3.9	355.1	24.2	30.1	12.5	28.9	3.00	1.00
2005	3	26	6	25	31.8	643.2	16.5	658.0	2.0	66.5	15.3	12.9	2.96	0.98
2005	3	2	18	43	30.0	635.6	22.4	607.3	62.3	59.6	21.4	19.1	2.81	0.92
2005	3	2	19	56	33.6	589.1	19.9	612.7	9.8	61.2	18.9	18.9	2.81	0.91
2005	3	31	5	36	19.0	432.0	8.7	464.8	3.5	44.0	5.0	22.7	2.83	0.92
2005	3	3	3	12	0.4	420.0	8.0	584.3	−13.9	45.8	16.4	42.0	2.96	0.98
2005	3	5	23	43	58.8	229.1	2.6	392.5	−6.1	22.7	1.4	53.2	2.16	0.53
2005	3	7	16	21	9.6	460.9	10.4	657.4	−15.6	49.3	80.7	43.5	2.83	0.92
2005	3	7	16	23	6.1	662.3	26.8	657.4	48.3	68.9	81.0	20.8	2.83	0.92
2005	3	7	9	53	44.9	579.1	17.0	635.2	−22.9	60.5	17.7	18.5	2.85	0.93
2005	3	9	17	2	59.2	351.8	5.1	699.2	−24.5	41.5	149.9	57.4	2.90	0.95
2005	3	9	20	56	33.5	713.5	28.2	699.5	50.5	72.0	15.0	18.4	2.82	0.92

Table A1. Continued.

yyyy	mm	dd	hh	mm	ss	V_t	$V_{t,err}$	V_{sw}	V_{pf}	$V_{pf,err}$	$\Delta\varphi$	θ	QG	QR
2005	3	9	21	24	10.6	421.9	8.0	672.7	−12.3	43.4	136.5	49.8	2.81	0.92
2005	4	10	2	35	3.1	304.3	4.7	328.1	−7.5	31.9	112.5	18.1	2.91	0.95
2005	4	10	5	0	14.7	184.3	1.5	322.1	8.5	18.9	83.1	56.9	2.96	0.98
2005	4	12	23	0	44.5	468.4	9.1	535.5	−4.6	49.1	3.1	27.8	2.37	0.65
2005	4	14	13	26	19.1	412.5	8.0	517.0	−85.2	50.6	83.2	15.3	2.81	0.91
2005	4	14	23	4	3.3	416.1	7.4	501.5	−24.7	44.2	37.2	28.4	2.95	0.98
2005	4	15	1	45	2.6	258.6	3.6	477.9	23.2	25.1	13.9	60.5	2.93	0.97
2005	4	24	12	30	29.7	428.1	9.5	541.6	14.5	42.5	15.9	40.2	2.95	0.98
2005	4	24	9	22	56.8	330.5	6.2	532.8	50.7	25.8	8.3	58.3	2.91	0.96
2005	4	29	9	49	55.0	297.0	4.0	334.3	−37.1	33.5	1.6	1.4	2.85	0.92
2005	4	29	9	54	3.9	437.6	8.6	334.1	106.0	34.1	5.8	6.7	2.84	0.91
2005	4	4	22	14	21.3	606.8	16.3	598.4	127.2	52.1	91.3	36.6	2.87	0.94
2005	4	5	11	22	18.7	357.4	5.4	639.1	33.8	34.9	137.6	59.5	2.96	0.98
2005	4	5	22	0	48.4	609.3	16.2	629.2	−14.7	63.0	5.3	5.9	2.06	0.46
2005	4	7	23	1	45.2	375.0	5.4	402.9	4.0	36.4	3.2	22.9	2.92	0.96
2005	4	7	4	52	5.5	356.4	5.1	470.4	81.9	25.0	132.7	54.3	2.93	0.97
Outliers														
2005	2	8	0	35	22.1	507.9	174.4	737.4	337.3	305.2	140.3	74.6	1.56	0.03
2005	2	8	0	37	0.0	559.3	160.7	737.4	270.2	299.7	141.4	60.4	1.56	0.03
2005	2	8	0	47	44.6	523.6	253.8	740.2	219.9	383.2	10.2	40.0	1.54	0.01

All velocities (V^*) are in units of km s^{-1}, and $\Delta\Phi$ and θ are in the unit of degrees. θ is the angle between the normal and the solar wind, and QG and QR are the tetrahedra quality factors described by Robert et al. (1998).

Data availability. Cluster measurements can be found through https://csa.esac.esa.int/csa-web/ (Laakso et al., 2010; Cluster team, 2022). The dates and times are listed in Table 1 in the Appendix.

Author contributions. HT initiated the study, performed the data analysis, and wrote the paper. All co-authors contributed to the analysis of the results and to the reviewing and editing of the paper

Competing interests. The contact author has declared that none of the authors has any competing interests.

Disclaimer. Publisher's note: Copernicus Publications remains neutral with regard to jurisdictional claims in published maps and institutional affiliations.

Acknowledgements. We thank the Cluster team for providing data and support. We acknowledge the use of the ESA Cluster Science Archive. We are thankful for the ESA Archival Research Visitor Programme. We acknowledge the use of the irfu-matlab package found through https://github.com/irfu/irfu-matlab (last access: 22 February 2023, Irfu-Matlab team, 2023). We are also thankful for the useful discussions with the International Space Sciences Institute (ISSI) team "Towards a Unifying Model for Magnetic Depressions in Space Plasmas". Henriette Trollvik and Tomas Karlsson are supported by the Swedish National Space Agency (SNSA) grant no. 190/19. Savvas Raptis and Tomas Karlsson are supported by the SNSA grant no. 90/17.

Financial support. This research has been supported by the Swedish National Space Agency (grant nos. 190/19 and 90/17).

Review statement. This paper was edited by Nick Sergis and reviewed by Martin Volwerk and Hadi Madanian.

References

Avinash, K. and Zank, G.: Magnetic structures in the heliosheath, Geophys. Res. Lett., 34, 5, https://doi.org/10.1029/2006GL028582, 2007.

Balogh, A., Dunlop, M., Cowley, S., Southwood, D., Thomlinson, J., Glassmeier, K., Musmann, G., Lühr, H., Buchert, S., Acuña,

M. H., Fairfield, D. H., Slavin, J. A., Riedler, W., Schwingenschuh, K., and Kivelson, M. G.: The Cluster magnetic field investigation, Space Sci. Rev., 79, 65–91, 1997.

Briand, C., Soucek, J., Henri, P., and Mangeney, A.: Waves at the electron plasma frequency associated with solar wind magnetic holes: STEREO/Cluster observations, J. Geophys. Res.-Space, 115, A12, https://doi.org/10.1029/2010JA015849, 2010.

Burlaga, L. F.: Micro-scale structures in the interplanetary medium, Sol. Phys., 4, 67–92, 1968.

Buti, B., Tsurutani, B., Neugebauer, M., and Goldstein, B.: Generation mechanism for magnetic holes in the solar wind, Geophys. Res. Lett., 28, 1355–1358, 2001.

Cluster team: Cluster Science Archive, ESA [data set], https://csa.esac.esa.int/csa-web/, last access: 10 October 2022.

Décréau, P., Fergeau, P., Krannosels'Kikh, V., Lévêque, M., Martin, P., Randriamboarison, O., Sené, F., Trotignon, J., Canu, P., Mögensen, P. B., and whisper investigators: WHISPER, a resonance sounder and wave analyser: Performances and perspectives for the Cluster mission, The Cluster and Phoenix Missions, Springer, 157–193, https://doi.org/10.1023/A:1004931326404, 1997.

Goodrich, K. A., Bonnell, J. W., Curry, S., Livi, R., Whittlesey, P., Mozer, F., Malaspina, D., Halekas, J., McManus, M., Bale, S., Bowen, T., Case, A., Dudok de Wit, T., Goetz, K., Harvey, P., Kasper, J., Larson, D., MacDowall, R., Pulupa, M., and Stevens, M.: Evidence of subproton-scale magnetic holes in the Venusian magnetosheath, Geophys. Res. Lett., 48, e2020GL090329, https://doi.org/10.1029/2020GL090329, 2021.

Gosling, J.: Magnetic reconnection in the solar wind, Space Sci. Rev., 172, 187–200, 2012.

Harvey, C. C.: Spatial gradients and the volumetric tensor, ISSI Sci. Rep. Ser., 1, 307–322, 1998.

Horbury, T., Lucek, E., Balogh, A., Dandouras, I., and Reme, H.: Motion and orientation of magnetic field dips and peaks in the terrestrial magnetosheath, J. Geophys. Res.-Space, 109, A9, https://doi.org/10.1029/2003JA010237, 2004.

Irfu-Matlab team: Irfu-MatLab repository, Github [data set], https://github.com/irfu/irfu-matlab, last access: 22 February 2023.

Karlsson, T., Heyner, D., Volwerk, M., Morooka, M., Plaschke, F., Goetz, C., and Hadid, L.: Magnetic holes in the solar wind and magnetosheath near Mercury, J. Geophys. Res.-Space, 126, e2020JA028961, https://doi.org/10.1029/2020JA028961, 2021.

Knetter, T.: A new perspective of the solar wind micro-structure due to multi-point observations of discontinuities, PhD Thesis, Universität zu Köln, https://kups.ub.uni-koeln.de/1508/ (last access: 15 February 2023), 2005.

Laakso, H., Perry, C., McCaffrey, S., Herment, D., Allen, A. J., Harvey, C. C., Escoubet, C. P., Gruenberger, C., Taylor, M. G. G. T., and Turner, R.: Cluster active archive: Overview, Springer, https://csa.esac.esa.int/csa-web/, 2010.

Madanian, H., Halekas, Jasper, S., Mazelle, Christian, X., Omidi, N., Espley, Jared, R., Mitchell, David, L., and Mcfadden, J. P.: Magnetic holes upstream of the Martian bow shock: MAVEN observations, J. Geophys. Res.-Space, 125, e2019JA027198, https://doi.org/10.1029/2019JA027198, 2020.

Rème, H., Aoustin, C., Bosqued, J. M., Dandouras, I., Lavraud, B., Sauvaud, J. A., Barthe, A., Bouyssou, J., Camus, Th., Coeur-Joly, O., Cros, A., Cuvilo, J., Ducay, F., Garbarowitz, Y., Medale, J. L., Penou, E., Perrier, H., Romefort, D., Rouzaud, J., Vallat, C., Alcaydé, D., Jacquey, C., Mazelle, C., d'Uston, C., Möbius, E., Kistler, L. M., Crocker, K., Granoff, M., Mouikis, C., Popecki, M., Vosbury, M., Klecker, B., Hovestadt, D., Kucharek, H., Kuenneth, E., Paschmann, G., Scholer, M., Sckopke, N., Seidenschwang, E., Carlson, C. W., Curtis, D. W., Ingraham, C., Lin, R. P., McFadden, J. P., Parks, G. K., Phan, T., Formisano, V., Amata, E., Bavassano-Cattaneo, M. B., Baldetti, P., Bruno, R., Chionchio, G., Di Lellis, A., Marcucci, M. F., Pallocchia, G., Korth, A., Daly, P. W., Graeve, B., Rosenbauer, H., Vasyliunas, V., McCarthy, M., Wilber, M., Eliasson, L., Lundin, R., Olsen, S., Shelley, E. G., Fuselier, S., Ghielmetti, A. G., Lennartsson, W., Escoubet, C. P., Balsiger, H., Friedel, R., Cao, J.-B., Kovrazhkin, R. A., Papamastorakis, I., Pellat, R., Scudder, J., and Sonnerup, B.: First multispacecraft ion measurements in and near the Earth's magnetosphere with the identical Cluster ion spectrometry (CIS) experiment, Ann. Geophys., 19, 1303–1354, https://doi.org/10.5194/angeo-19-1303-2001, 2001.

Robert, P., Roux, A., Harvey, C. C., Dunlop, M. W., Daly, P. W., and Glassmeier, K.-H.: Tetrahedron geometric factors, Anal. Method. Multi-Spacecr. Data, 1, 323–328, 1998.

Rosenblatt, M.: Remarks on some nonparametric estimates of a density function, The annals of mathematical statistics, 27, 832–837, 1956.

Southwood, D. J. and Kivelson, M. G.: Mirror instability: 1. Physical mechanism of linear instability, J. Geophys. Res.-Space, 98, 9181–9187, 1993.

Sperveslage, K., Neubauer, F., Baumgärtel, K., and Ness, N.: Magnetic holes in the solar wind between 0.3 AU and 17 AU, Nonl. Process. Geophys., 7, 191–200, 2000.

Sundberg, T., Burgess, D., and Haynes, C.: Properties and origin of subproton-scale magnetic holes in the terrestrial plasma sheet, J. Geophys. Res.-Space, 120, 2600–2615, 2015.

Tsurutani, B., Dasgupta, B., Galvan, C., Neugebauer, M., Lakhina, G., Arballo, J., Winterhalter, D., Goldstein, B., and Buti, B.: Phase-steepened Alfvén waves, proton perpendicular energization and the creation of magnetic holes and magnetic decreases: The ponderomotive force, Geophys. Res. Lett., 29, 86–1, https://doi.org/10.1029/2002GL015652, 2002.

Tsurutani, B. T., Lakhina, G. S., Verkhoglyadova, O. P., Echer, E., Guarnieri, F. L., Narita, Y., and Constantinescu, D. O.: Magnetosheath and heliosheath mirror mode structures, interplanetary magnetic decreases, and linear magnetic decreases: Differences and distinguishing features, J. Geophys. Res.-Space, 116, A2, https://doi.org/10.1029/2010JA015913, 2011.

Turner, J., Burlaga, L., Ness, N., and Lemaire, J.: Magnetic holes in the solar wind, J. Geophys. Res., 82, 1921–1924, 1977.

Volwerk, M., Goetz, C., Plaschke, F., Karlsson, T., Heyner, D., and Anderson, B.: On the magnetic characteristics of magnetic holes in the solar wind between Mercury and Venus, Ann. Geophys., 38, 51–60, https://doi.org/10.5194/angeo-38-51-2020, 2020.

Wang, M., Yao, S., Shi, Q., Zhang, H., Tian, A., Degeling, A. W., Zhang, S., Guo, R., Sun, W., Liu, J., Bai, S., Shen, X., Zhu, X., Fu, S., and Pu, Z.: Propagation properties of foreshock cavitons: Cluster observations, Sci. China Technol. Sci., 63, 173–182, 2020.

Winterhalter, D., Neugebauer, M., Goldstein, B. E., Smith, E. J., Bame, S. J., and Balogh, A.: Ulysses field and plasma observations of magnetic holes in the solar wind and their relation to mirror-mode structures, J. Geophys. Res.-Space, 99, 23371–23381, 1994.

Xiao, T., Shi, Q. Q., Zhang, T. L., Fu, S. Y., Li, L., Zong, Q. G., Pu, Z. Y., Xie, L., Sun, W. J., Liu, Z. X., Lucek, E., and Reme, H.: Cluster-C1 observations on the geometrical structure of linear magnetic holes in the solar wind at 1 AU, Ann. Geophys., 28, 1695–1702, https://doi.org/10.5194/angeo-28-1695-2010, 2010.

Zhang, T., Russell, C., Baumjohann, W., Jian, L., Balikhin, M., Cao, J., Wang, C., Blanco-Cano, X., Glassmeier, K.-H., Zambelli, W., Volwerk, M., Delva, M., and Vörös, Z.: Characteristic size and shape of the mirror mode structures in the solar wind at 0.72 AU, Geophys. Res. Lett., 35, 10, https://doi.org/10.1029/2008GL033793, 2008.

Zurbuchen, T., Hefti, S., Fisk, L., Gloeckler, G., Schwadron, N., Smith, C., Ness, N., Skoug, R., McComas, D., and Burlaga, L.: On the origin of microscale magnetic holes in the solar wind, J. Geophys. Res.-Space, 106, 16001–16010, 2001.